DAILY QA
Finished before your first cup of coffee

MONTHLY QA
Never re-learn workflow again

ANNUAL QA
Confidence with fewer gray hairs

STEREOTACTIC
When millimeters matter most

ABSOLUTE DOSIMETRY
"Pinpoint" is our margin of error

PATIENT DOSIMETRY
Pre-treatment is just the beginning

QA Solutions. ***Our expertise is at your service.***

STANDARD IMAGING®

MORE THAN JUST QA PRODUCTS, FIND QA SOLUTIONS AT

www.standardimaging.com

1411-00_2/18

Simultaneous estimation and segmentation from projection data in dynamic PET

Jianan Cui, Haiqing Yu, and Shuhang Chen
State Key Laboratory of Modern Optical Instrumentation, College of Optical Science and Engineering, Zhejiang University, Hangzhou 310027, China

Yunmei Chen
Department of Mathematics, University of Florida, 458 Little Hall, Gainesville, FL32611-8105, USA

Huafeng Liu[a)]
State Key Laboratory of Modern Optical Instrumentation, College of Optical Science and Engineering, Zhejiang University, Hangzhou 310027, China

(Received 22 February 2018; revised 17 December 2018; accepted for publication 17 December 2018; published 4 February 2019)

Purpose: Dynamic positron emission tomography (PET) is known for its ability to extract spatiotemporal information of a radio tracer in living tissue. Information of different functional regions based on an accurate reconstruction of the activity images and kinetic parametric images has been widely studied and can be useful in research and clinical setting for diagnosis and other quantitative tasks. In this paper, our purpose is to present a novel framework for estimating the kinetic parametric images directly from the raw measurement data together with a simultaneous segmentation accomplished through kinetic parameters clustering.

Method: An iterative framework is proposed to estimate the kinetic parameter image, activity map and do the segmentation simultaneously from the complete dynamic PET projection data. The clustering process is applied to the kinetic parameter variable rather than to the traditional activity distribution so as to achieve accurate discrimination between different functional areas. Prior information such as total variation regularization is incorporated to reduce the noise in the PET images and a sparseness constraint is integrated to guarantee the solution for kinetic parameters due to the over complete dictionary. Alternating direction method of multipliers (ADMM) method is used to solve the optimization problem. The proposed algorithm was validated with experiments on Monte Carlo-simulated phantoms and real patient data. Symbol error rate (SER) was defined to evaluate the performance of clustering. Bias and variance of the reconstruction activity images were calculated based on ground truth. Relative mean square error (MSE) was used to evaluate parametric results quantitatively.

Result: In brain phantom experiment, when counting rate is 1×10^6, the bias (variance) of our method is 0.1270 (0.0281), which is lower than maximum likelihood expectation maximization (MLEM) 0.1637 (0.0410) and direct estimation without segmentation (DE) 0.1511 (0.0326). In the Zubal phantom experiment, our method has the lowest bias (variance) 0.1559 (0.0354) with 1×10^5 counting rate, compared with DE 0.1820 (0.0435) and MLEM 0.3043 (0.0644). As for classification, the SER of our method is 18.87% which is the lowest among MLEM + k-means, DE + k-means, and kinetic spectral clustering (KSC). Brain data with MR reference and real patient results also show that the proposed method can get images with clear structure by visual inspection.

Conclusion: In this paper, we presented a joint reconstruction framework for simultaneously estimating the activity distribution, parametric images, and parameter-based segmentation of the ROIs into different functional areas. Total variation regularization is performed on the activity distribution domain to suppress noise and preserve the edges between ROIs. An over complete dictionary for time activity curve basis is constructed. SER, bias, variance, and MSE were calculated to show the effectiveness of the proposed method. [https://doi.org/10.1002/mp.13364]

Key words: dynamic PET, kinetic model, PET reconstruction, segmentation

1. INTRODUCTION

Compared with static PET, which only deals with the value of concentration within a fixed period of time, the emergence of dynamic PET has made it possible to track temporal changes in activity distribution and to provide an estimation of tracer kinetics.[1] With the additional temporal information, the underlying biological and physiological process in a

living tissue can be collected noninvasively and evaluated quantitatively, which has long been proved useful in various areas of medical and clinical research,[2–4] such as tumor diagnosis and therapy monitoring, that utilize the predictability of the kinetic values.[5,6]

Conventionally, estimation and segmentation for parametric images are performed individually. An accurate estimation is required as a primary step for segmentation. In traditional approaches, kinetic parameters are estimated by mathematically modeling the tracer in the living tissue and solving the inverse problem with or without prior knowledge of the radio activity distribution. In the case of direct estimation[8–10], the tracer kinetics can be estimated directly from the raw projection data, allowing better modeling of the noise and hence achieving a more accurate image result compared to that obtained via indirect methods, in which the activity images are first reconstructed and then the estimation problem based on the preceding result of the PET images is solved. Because of the low signal-to-noise ratio (SNR) at each measurement, failing to incorporate the information from multiple time frames may lead to enhanced noise in the dynamic activity images which is expected to further propagate to the parametric image estimates in the indirect reconstruction scheme. There has been a significant amount of research focused on the estimation of tracer kinetics from both direct and indirect methods.[11,12] Right after the application of MLEM was introduced into the static PET reconstruction problem, Snyder et al. first estimated the compartmental parameters in 1984 directly from the raw measurement data using the MLEM method.[13] Kamasak et al. in 2005 described a penalized likelihood estimation algorithm of parametric images that incorporated the two-tissue compartment model.[14] In 2008, Yan et al. proposed a MLEM-based reconstruction algorithm for kinetic parameters by applying the one-tissue compartment model.[15] Note that both Kamasak and Yan have chosen the compartmental model to fit the tracer kinetics. Since the model fitting is an essential step for the estimation of kinetic parameters, Wang and Qi summarized a generalized algorithm to directly reconstruct the parametric images that can be implemented with linear or nonlinear kinetic models.[2,16]

In PET image processing, delineating the outline of the functional regions for PET data is a complicated and time-consuming problem. The boundary information of each functional region can be used to suppress the noise corruption, which is a key feature for the indirect methods that treat the PET reconstruction and segmentation as two individual methods. In direct reconstruction, most work has focused on incorporating spatial smoothing priors into a MAP reconstruction framework.[17,18] With prior knowledge of the region of interest (ROI), noise corruption in the imaging field can be reduced, thus enhancing the quality of the reconstruction results.[19–22]

Recently, the underlying connection between reconstruction and segmentation has been widely recognized. In 2006, Reader et al. presented a reconstruction scheme for joint estimation of the activity distributions and temporal basis functions of the tracer kinetics scheme, solving the problem through a MLEM-based scheme in conjunction with a model-fitting process.[23] Saad et al. in 2007 published their algorithm that can simultaneously export the delineation result and kinetic parameter estimation in Ref. [24]. Later, in 2008, Krestyannikov et al. achieved ROI segmentation and estimated the corresponding time activity curves within each function area at the same time through a statistical approach.[25] Sungwon et al. proposed an iterative algorithm that can simultaneously segment and reconstruct for tomographic images.[26] The basic strategy of the proposal algorithms is to solve the problem with multiple underdetermined variables, by either alternating the unknown estimates, or by using mathematical methods to reduce the number of unknowns.

In this paper, we proposed a direct estimation scheme for parametric images with simultaneous segmentation and reconstruction of the activity distribution. Unlike either direct or indirect approaches, in this work, PET activity images were achieved jointly during the estimation of kinetic parameters, therefore an additional regularization of temporal information based on the tracer kinetics could be included to improve the image accuracy. For PET images, total variation regularization was incorporated to increase the accuracy of activity distribution. For direct estimation of kinetic parameters, based on the compartmental model theory, a dictionary containing possible time activity curves (TACs) basis was defined and an extra sparse constraint was added to confirm the solution of the problem, which has been used in Ref. [8]. The cluster-based within-class scatter matrix and initial knowledge of the ROIs were given by the Dirichlet process clustering algorithm.[27] The whole simultaneous reconstruction and segmentation framework was solved by the ADMM method using an alternating iterative scheme. The performance and clinical value of the proposed method were evaluated using Monte Carlo-simulated phantom data, MRI registration data, and real patient data.

2. PROBLEM STATEMENT

2.A. Image Reconstruction

During an emission PET scan, the process in which two photons generated through the annihilation of positrons emitted from the tracer are detected by an opposite probe pair is called a coincidence event. In PET imaging, however, the true coincidence events are often contaminated with random coincidence (RC) events and scattered coincidence (SC) events. The raw projection data of dynamic PET (called a sinogram) $Y \in \mathbb{R}^{I \times M}$ is organized as an array of coincidence events y_{im} collected by all the I detector pairs indexed by $i = 1,\ldots,I$ from the first time frame till the last Mth time frame, noted as $m = 1,\ldots,M$. Within the measurement sinogram, single projection data can be well modeled by a linear Poisson model:

$$y_{im} \sim \text{Poisson}\{\overline{y}_{im}\} \tag{1}$$

Expectation $\bar{y}_{im}$ is connected to the unknown tracer distribution $\{x_{jm}\}$ at time frame m through the affine transform:

$$\bar{y}_{im} = \sum_{j=1}^{J} g_{ij} x_{jm} + r_{im} + s_{im}, \tag{2}$$

in which J is the number of discrete pixels in the activity distribution field. g_{ij} is the (i,j)th entry of the system matrix $G \in \mathbb{R}^{I \times J}$ representing the average probability that the photon emitted from pixel j interacted detector pair i. x_{jm} is the concentration value at jth pixel in time frame m. r_{im} and s_{im} account for the presence of random and scatter coincidence in the ith detector pair. Given that the detection at each probe can be considered as an independent process, the dynamic PET data can also be well modeled as a collection of independent Poisson random variables:

$$\text{Prob}(Y|X) = \prod_{m=1}^{M} \prod_{i=1}^{I} e^{-\bar{y}_{im}} \frac{\bar{y}_{im}^{\,y_{im}}}{y_{im}!}. \tag{3}$$

A well-known procedure would be maximizing the likelihood function.[29] However, in this study, we chose to take the negative logarithm function, and the reconstruction of X:$X \in \mathbb{R}^{J \times M}$ is therefore achieved when minimizing the problem:

$$\mathcal{L}^{temp}(X) = \sum_{m=1}^{M} \sum_{i=1}^{I} (\bar{y}_{im} - y_{im} \log \bar{y}_{im}) \tag{4}$$

Additionally, total variation (TV) regularization[30] is composed on the solution for X

$$\mathcal{L}(X) = TV(X) + \alpha \sum_{m=1}^{M} \sum_{i=1}^{I} (\bar{y}_{im} - y_{im} \log \bar{y}_{im}) \tag{5}$$

in which α is the weighting parameter for the negative Poisson log-likelihood function and $TV(X)$ refers to the total variation regularization. By using the dual form of total variation, the term $TV(X)$ can be calculated through

$$TV(X) = \sum_{m=1}^{M} \sum_{j=1,}^{J} \left\| (D\mathbf{x}_m)_j \right\|, \tag{6}$$

where $\mathbf{x}_m \in \mathbb{R}^J$ is the component of X referring to the activity distribution for the mth time frame and $(D\mathbf{x}_m)_j \in \mathbb{R}^2$ is defined as the discrete gradient of $\mathbf{x}_m$ at the jth pixel.

2.B. Kinetic modeling

The tracer kinetics can be well modeled by the compartmental model since it is easy to implement and closely related to the underlying metabolism.[31] A typical tracer-exchange process of the two-tissue compartment model is shown in Fig. 1, where C_P, C_F, and C_B denote the concentration of the plasma, the tracer that has not been involved in metabolism, and the labeled metabolite, respectively. C_T is the sum of the concentration in the target tissue corresponding to the input function C_P. A general equation for C_T can be expressed as

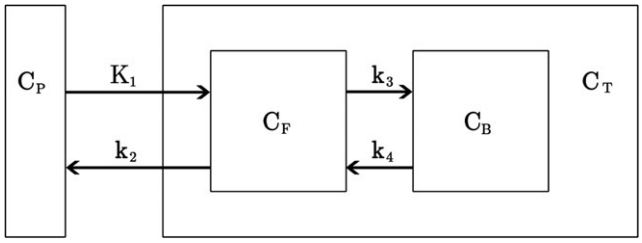

FIG. 1. Two-tissue compartment models characterized by two differential equations: $C_F(t)$:$dC_F(t)/dt = K_1C_P(t) - k_2C_F(t) - k_3C_F(t) + k_4C_B(t)$; $C_B(t)$: $dC_B(t)/dt = k_3C_F(t) - k_4C_B(t)$, with K_1,k_2,k_3,k_4 being the exchange rate constants.

$$C_T(t) = \left[\phi_0 \delta(t) + \sum_{q=1}^{Q} \phi_q e^{-\theta_q t} \right] \otimes C_P(t), \tag{7}$$

where $\otimes$ is the convolution operator, t is the time interval, ϕ_q and θ_q are the coefficients in the function of $C_T(t)$ representing the weighting parameter and the exponent parameter for each tissue compartment q =1,. . .,Q in the target tissue, and $\delta(t)$ is defined as the delta function for the part of labeled tracer that is not involved in any of those two compartments. In this case, the unknown parameters that characterize kinetic modeling system have been transformed from exchange rate constants K_1,k_2,k_3,k_4 into two set of parameters ϕ_q and θ_q. To further simplify the equation, the expression for $C_T(t)$ is expanded as

$$\begin{aligned} C_T(t) &= \sum_{q=0}^{Q} \phi_q \psi_q(t) \\ \text{s.t. } \psi(t) &= \begin{cases} C_P(t), & q = 0, \\ \int_0^t e^{-\theta_q (t-\tau)} C_P(\tau) d\tau, & q = 1, \ldots, Q, \end{cases} \end{aligned} \tag{8}$$

Since dynamic PET measurement data are generated through continuous detection with a certain time interval for each time frame, the value of the jth pixel in the activity map for the mth time frame can be calculated as an integration of the total concentration from the starting time t_m^s to the ending time t_m^e, which is given by

$$x_{jm} = \frac{1}{t_m^e - t_m^s} \int_{t_m^s}^{t_m^e} C_T^j(t) dt, \tag{9}$$

where $C_T^j(t)$ is specifically defined as the concentration of the target tissue for the jth pixel. By substituting Eq. (8), the data-fitting process for the kinetic modeling and the activity distribution can be expressed as

$$\min_{X,\Phi} \|X - (\Psi\Phi)^T\|^2, \tag{10}$$

where the superscript ^{T} refers to the transpose of the matrix and $\|\cdot\|$ denotes the Euclidean norm. $\Psi \in \mathbb{R}^{M \times (N+1)}$, defined as the kinetic dictionary, is the matrix composed of the integration of kinetic basis functions with different compartmental parameter $\theta_c(c = 1,\ldots,N)$ corresponding to the data-sampling process. $\Phi \in \mathbb{R}^{(N+1) \times J}$ is the coefficient

matrix of the kinetic dictionary. $\Psi \in \mathbb{R}^{M\times(N+1)}$ can be written as follows:

$$\Psi = \begin{bmatrix} \psi_{10} & \psi_{11} & \cdots & \psi_{1N} \\ \vdots & \vdots & \vdots & \vdots \\ \psi_{M0} & \psi_{M1} & \cdots & \psi_{MN} \end{bmatrix}. \tag{11}$$

Each component in matrix Ψ is precalculated through

$$\psi_{mc} = \frac{1}{t_m^e - t_m^s} \times \begin{cases} \int_{t_m^s}^{t_m^e} C_P(t)dt, & c = 0, \\ \int_{t_m^s}^{t_m^e} \int_0^t e^{-\theta_c(t-\tau)} C_P(\tau)d\tau, & c = 1,\ldots,N. \end{cases} \tag{12}$$

Usually, the number N should be large enough to cover the essential kinetic spectrums; a large value of N will yield an over complete matrix Ψ and hence leave the problem with a number of underdetermined equations. The collection of $\theta = \{\theta_1 \ldots \theta_c \ldots \theta_N\}$ are discrete values within a physiologically plausible range (will be changed when the tracer is different) and the interval between two elements is set to be in a logarithmic manner covering a suitable range of the kinetic spectrum. Inspired by the underlying process described by the compartmental model in which only a few compartments are involved in describing the activity distribution in the field, an extra sparse constraint on the underdetermined coefficient Φ is introduced and further reformulating the minimizing problem for the kinetic model as

$$\mathcal{S}(X,\Phi) = \|X - (\Psi\Phi)^T\|^2 + \mu\|\Phi\|_1 \tag{13}$$

where μ is a relative weighting parameter for the sparse constraint and $\|\cdot\|_1$ refers to the standard ℓ_1 norm.

The rate constant, $K_1 \in \mathbb{R}^J$ can be computed from the estimation value of Φ according to Ref. [31]

$$(K_1)_j = \sum_{c=1}^{N} \phi_{cj}, \tag{14}$$

where $(K_1)_j$ is the jth component of K_1. In some cases, V_d can also calculated from the estimation value of Φ.

2.C. Kinetic parameter clustering

Segmentation in PET imaging can be achieved both on the domain of activity distribution[33] and using TAC clustering.[34] In a two-step segmentation procedure, reconstruction quality is essential to the accuracy of the following delineation. Unlike other advanced methods that focus on either primary image reconstruction or the subsequent region delineation, our method proposes a simultaneous clustering framework in the estimation problem. Due to the fact that the sparse coefficients of the TAC have been demonstrated as a more discriminative and robust feature than raw data,[35] we propose incorporating the within-class scatter matrix Φ from the Fisher discrimination criterion[36]

$$\begin{aligned} \mathcal{C}(\Phi) &= \sum_{h=1}^{H} \sum_{\phi_h \in C_h} (\phi_h - \rho_h)(\phi_h - \rho_h)^T \\ \text{s.t. } \rho_h &= \frac{1}{n_h} \sum_{\phi_h \in C_h} \phi_h, \end{aligned} \tag{15}$$

where $\phi_h \in \mathbb{R}^{N\times n_h}$ represents a subset of the coefficient matrix Φ that is related to the pixels within the hth cluster C_h, n_h is the number of pixels in the hth cluster, ρ_h represents the matrix composed of the average values of Φ for the hth cluster, and H is the number of clusters. The initial values of ρ_h and H are predetermined by the clustering algorithm with a Dirichlet process[37,38] and will be updated with respect to Φ during the optimizing process.

3. METHODS FOR JOINT RECONSTRUCTION

3.A. Objective function

By taking into consideration the kinetic modeling and incorporating the within-class scatter matrix Φ kinetic parameter clustering, our final objective function can be expressed as follows:

$$\begin{aligned} \mathcal{F}(X,\Phi) = TV(X) &+ \alpha \sum_{m=1}^{M}\sum_{i=1}^{I} (\bar{y}_{im} - y_{im}\log\bar{y}_{im}) \\ &+ \frac{\gamma}{2}(\|X - (\Psi\Phi)^T\|^2 + \mu\|\Phi\|_1 \\ &+ \epsilon \sum_{h=1}^{H} \sum_{\phi_h \in C_h} (\phi_h - \rho_h)(\phi_h - \rho_h)^T) \\ \text{s.t. } \rho_h &= \frac{1}{n_h} \sum_{\phi_h \in C_h} \phi_h, \quad \bar{y}_{im} = \sum_{j=1}^{J} g_{ij}x_{jm}, \end{aligned} \tag{16}$$

where ε is set as the relative weighting parameter for the clustering term of Φ.

3.B. Optimization framework

Basically, the main strategy of the proposal joint reconstruction and segmentation framework is to minimize the problem (14) by alternating between the update of variable X and Φ at every iteration. The subproblem for minimizing X while Φ is fixed is rewritten with the components that contain X as follows:

$$\begin{aligned} \mathcal{F}_X(X,\Phi) = TV(X) &+ \alpha \sum_{m=1}^{M}\sum_{i=1}^{I} (\bar{y}_{im} - y_{im}\log\bar{y}_{im}) \\ &+ \frac{\gamma}{2}\|X - (\Psi\Phi)^T\|^2 \quad \text{s.t. } \bar{y}_{im} = \sum_{j=1}^{J} g_{ij}x_{jm}. \end{aligned} \tag{17}$$

The alternating direction method of multipliers (ADMM)[39,40] is applied to estimate X by introducing a set of auxiliary variables w_{jm} to replace $(D\mathbf{x}_m)_j$, and the subproblem can be further transformed to

$$\mathcal{F}_X(X,\Phi)=\sum_{m=1}^{M}\sum_{j=1,}^{J}\|w_{jm}\|+\alpha\sum_{m=1}^{M}\sum_{i=1}^{I}(\bar{y}_{im}-y_{im}\log\bar{y}_{im})+\frac{\gamma}{2}\|X-(\Psi\Phi)^T\|^2\quad\text{s.t. }\bar{y}_{im}=\sum_{j=1}^{J}g_{ij}x_{jm}. \tag{18}$$

The corresponding augmented Lagrangian function for Eq. (18) can be expressed as

$$\begin{aligned}L_A(w_{jm},X)=&\sum_{j=1}^{J}(\|w_{jm}\|-v_{jm}^T((D\mathbf{x}_m)_j-w_{jm})\\&+\frac{\beta_{jm}}{2}\|(D\mathbf{x}_m)_j-w_{jm}\|^2)\\&+\alpha\sum_{m=1}^{M}\sum_{i=1}^{I}(\bar{y}_{im}-y_{im}\log\bar{y}_{im})\\&+\frac{\gamma}{2}\|X-(\Psi\Phi)^T\|^2\end{aligned} \tag{19}$$

in which $v_{jm}\in\mathbb{R}^{2\times 1}$ denotes the Lagrange multipliers, β_{jm} is the penalty parameters, and w_{jm} can be acquired from the two-dimensional (2D) shrinkage formula

$$w_{jm}^{k+1}=\max\{\|(D\mathbf{x}_m^k)_j-\frac{v_{jm}^k}{\beta_{jm}}\|-\frac{1}{\beta_{jm}},0\}\frac{(D\mathbf{x}_m^k)_j-\frac{v_{jm}^k}{\beta_{jm}}}{\|(D\mathbf{x}_m^k)_j-\frac{v_{jm}^k}{\beta_{jm}}\|}. \tag{20}$$

With the newly updated w_{jm}^{k+1}, X minimizes the following function:

$$\begin{aligned}L_A^{(X)}=&\sum_{j=1}^{J}(-v_{jm}^T(D\mathbf{x}_m)_j+\frac{\beta_{jm}}{2}\|(D\mathbf{x}_m)_j-w_{jm}^{k+1}\|^2)\\&+\alpha\sum_{m=1}^{M}\sum_{i=1}^{I}(\bar{y}_{im}-y_{im}\log\bar{y}_{im})+\frac{\gamma}{2}\|X-(\Psi\Phi)^T\|^2,\end{aligned} \tag{21}$$

where

$$\bar{y}_{im}=\sum_{j=1}^{J}g_{ij}x_{jm}. \tag{22}$$

Therefore, updating X can be achieved through

$$X^{k+1}=X^k-\rho_m^k d^k(X)X^k, \tag{23}$$

where ρ_m^k is the corresponding descent step length and is chosen to be the deepest step length computed by back-tracking the nonmonotonic line search scheme[41] that begins with the Barzilai–Borwein (BB) step length.[42] $d^k(X)$ is defined as the gradient of Eq. (21) as

$$\begin{aligned}d^k(X)=&\sum_{j=1}^{J}(-D^Tv_{jm}+\beta_{jm}D^T((D\mathbf{x}_m)_j-w_{jm}^{k+1}))\\&-M\alpha\sum_{i=1}^{I}\sum_{j=1}^{J}g_{ij}-\alpha\sum_{m=1}^{M}\sum_{i=1}^{I}\frac{y_{im}\sum_{j=1}^{Jg}ij}{\bar{y}_{im}}\\&+\gamma(X-(\Psi\Phi)^T).\end{aligned} \tag{24}$$

After each update of w_{jm} and X, the multipliers need to be modified as well. Based on the latest value of other variables, v_{jm} will be revised through

$$v_{jm}^{k+1}=v_{jm}^k-\beta\left((D\mathbf{x}_m^{k+1})_j-w_{jm}^{k+1}\right). \tag{25}$$

The process will end when the solution for both variables meets a prescribed tolerance. Before proceeding to the Φ subproblem, clustering with Dirichlet processes is first performed on the current estimation of Φ^k to renew the ROI information. Then the update of Φ is achieved through the following minimization problem composed of the Φ-relevant terms from Eq. (16):

$$\begin{aligned}\mathcal{F}_\Phi(X,\Phi)=&\frac{\gamma}{2}(\|X-(\Psi\Phi)^T\|^2+\mu\|\Phi\|_1\\&+\epsilon\sum_{h=1}^{H}\sum_{\phi_h\in C_h}(\phi_h-\rho_h)^T(\phi_h-\rho_h))\\\text{s.t.}\quad&\rho_h=\frac{1}{n_h}\sum_{\phi_h\in C_h}\phi_h.\end{aligned} \tag{26}$$

Notice that the minimization problem (26) can be simplified and decomposed as follows:

$$\begin{aligned}\mathcal{F}_\Phi(X,\Phi)=&\frac{\gamma}{2}\sum_{h=1}^{H}\mathcal{F}_\Phi^h(x_h,\phi_h)\\\text{s.t.}\quad\mathcal{F}_\Phi^h(x_h,\phi_h)=&\|x_h-(\Psi\phi_h)^T\|^2+\mu\|\phi_h\|_1\\&+\epsilon\sum_{\phi_h\in C_h}(\phi_h-\rho_h)^T(\phi_h-\rho_h),\end{aligned} \tag{27}$$

where x_h and ϕ_h are, respectively, defined as the collection of all the rows (in the case of X) or columns (in the case of Φ) that belong to the hth cluster. Labels for each column of Φ are determined using spectral clustering upon the current estimate of Φ^k[35,43] To further simplify (27), assume E_h is a matrix of size $n_h\times n_h$ with all entries being 1, where n_h is the number of voxels in the hth cluster, I_h refers to the unitary matrix of the same size with E_h, and $N_h=I_h-E_h/n_h$. Therefore, we get the equivalent expression

$$\begin{aligned}&\mathcal{F}_\Phi^h(x_h,\phi_h)=\mu\|\phi_h\|_1+\mathcal{Q}_h(x_h,\phi_h)\\s.t.\quad&\mathcal{Q}_h(x_h,\phi_h)=\|x_h-(\Psi\phi_h)^T\|^2+\epsilon\|\phi_hN_h\|^2.\end{aligned} \tag{28}$$

By linearizing the two terms in $\mathcal{Q}_h(x_h,\phi_h)$ at ϕ_h, adding the proximal term $\frac{1}{2\sigma}\|\phi_h-\phi_h^k\|^2$, and then iteratively using the shrinkage operator we can get

$$\phi_h^{k+1}=\mathbf{S}_{\mu/\sigma}\left(\phi_h^k-\frac{1}{2\sigma}\nabla\mathcal{Q}_h(x_h^k,\phi_h)\right), \tag{29}$$

where $\mathbf{S}_{\mu/\sigma}$ is the soft shrinkage operator[44] and $\nabla\mathcal{Q}_h(x_h,\phi_h)$ is given by

$$\nabla\mathcal{Q}_h(x_h,\phi_h)=-2\Psi^T(x_h-(\Psi\phi_h)^T)+2\epsilon(\phi_hN_h)N_h^T. \tag{30}$$

An overview of the whole joint reconstruction framework is demonstrated in Algorithm 1.

Algorithm 1 Iterative optimization scheme of the proposed model

Require Sinogram Y, system matrix G, dictionary Ψ, and input weighting parameters, α, γ, μ, ε.

1: **Initialize** Iteration number $k = 1$

2: **repeat**

3: $w_{jm}^{k+1} \leftarrow \arg\min L_A^{(w_{jm})}$ with X^k, v_{jm}^k

4: $X^{k+1} \leftarrow \arg\min L_A^{(X)}$ with w_{jm}^{k+1}, v_{jm}^k

5: $v_{jm}^{k+1} \leftarrow v_{jm}^k - \beta((D\mathbf{x}_m^{k+1})_j - w_{jm}^{k+1})$

6: Cluster Φ

7: Update Φ^{k+1} with soft thresholding operator $\mathbf{S}_{\mu/\sigma}$.

8: **until** Relative changes of both X, Φ $<10^{-3}$ are satisfied

9: **Return** Φ, X, and the segmentation results.

4. EXPERIMENTS AND RESULTS

In the following sections, the proposed joint reconstruction framework will be tested on Monte Carlo-simulated Zubal, brain phantom data, and a set of measurement data provided from a local hospital. The proposed method is performed in a desktop computer with i7 Intel Core CPU and 8 GB RAM.

Experimental results are presented both visually and quantitatively. Other than intuitive visual images, we use following criteria to further illuminate the improvements in the reconstruction accuracy.

$$\begin{aligned} \text{bias} &= \frac{1}{M}\sum_{m=1}^{M}\left(\frac{1}{J}\sum_{j=1}^{J}\frac{|\hat{x}_{jm} - x_{jm}|}{x_{jm}}\right), \\ \text{variance} &= \frac{1}{M}\sum_{m=1}^{M}\left(\frac{1}{J-1}\sum_{j=1}^{J}\left(\frac{\hat{x}_{jm} - \bar{x}_{jm}}{x_{jm}}\right)^2\right), \end{aligned} \tag{31}$$

where x_{jm}, $\hat{x}_{jm}$, and $\bar{x}_{jm}$ denote the true value, reconstructed value, and the mean value within the same cluster for pixel site j at time frame m. For the parametric image of K_1, a relative mean square error (MSE) is calculated for comparison. In addition, inspired by the symbol error rate (SER) in digital communications, we define the assessment standard for the clustering procedure as the cluster error rate

$$\text{SER} = \frac{N_e}{J} \times 100\% \tag{32}$$

in which N_e is the number of pixels that have been clustered into the wrong area.

Results achieved by the proposal method are presented under the abbreviation SDES, short for simultaneous direct estimation and segmentation. To test the improvement of the clustering term in Eq. (15), an inferior version of the proposed framework which excluded the clustering part has also been conducted for the comparison of PET images and kinetic parameters under the abbreviation of DE, short for direct estimation. In addition, maximum likelihood expectation maximization (MLEM) method is incorporated for the comparison of PET activity distribution. Based on the results of MLEM reconstruction images, an indirect estimation approach of kinetic parameters, known as data-driven estimation of parametric images based on compartmental theory (DEPICT),[32] is introduced for comparison. As for the clustering part, a well-known k-means clustering method[49] is applied on MLEM reconstruction images for the comparison of segmentation results, shortened as KMC in this paper. Also, a kinetic spectral clustering method (KSC)[34] which carries out segmentation based on TAC is used as comparison.

4.A. Implementation of tunable parameters

In this joint reconstruction scheme, there are four tunable parameters (α, γ, μ and ε) that need to be predetermined manually. The values for these parameters are determined basically by evaluating the performance of the proposed framework. The principle of the tuning process is while the underdetermined parameter is being tuned, other three are fixed as a relatively suitable value based on the existing research.

The α is a relative weighting parameter for the negative log-likelihood term which is closely related to the noise level and should be smaller if the noise corruption in the measurement data is strong. Based on the default value of α in Li,[45] experiments under different values of $\alpha \in \{2^5, 2^6, 2^{6.5}, 2^7, 2^8\}$ have been firstly conducted to find a relatively suitable value of α. From the image profiles shown in Supplemental Fig. S1, we found that the optimal reconstruction result is yielded when α is settled as $2^{6.5}$. Secondly, a set of experiments is designed for parameter γ. Since we cannot find an analogue of the proposed framework, the results of eight sets of reconstruction experiments with respect to $\gamma \in \{0.1,0.33,0.66,1,1.33,1.66,2.33\}$ have been assessed. Supplemental Fig. S2(a) and S2(b) present the curves of relative bias and variance (for PET images) and the curve of MSE (for parametric images) with respect to the value of γ, respectively. In consequence, the value of γ is fixed at the potentially lowest position on the curve, that is, $\gamma = 0.6$. Next, similar experiments have been performed relating to the parameters μ and ε. According to the research in Ref. [32] and the range of relative MSE, over the experiments with $\mu \in \{0.01,0.03,0.06,0.10\}$, the value of μ that we used in all experiments is 0.06. Lastly the choice of ε is within the range of $\{0.5,1,2,3\}$ and is settled with 0.5. Experiments regarding μ and ε can be found in Supplemental Fig. S3 and S4.

4.B. Monte Carlo-simulated data

Monte Carlo simulation is able to replicate the physical process of PET imaging and produce the realistic

measurement sinogram data for evaluating PET reconstruction algorithms. With ground truth being known, the reconstruction results of Monte Carlo-simulated data can be compared with highly reliable criteria. In this case, the simulation is performed on two sets of data sequences generated from brain and the Zubal thorax phantom.

4.B.1 Hoffman brain phantom

First, we conduct the experiments on Hoffman brain phantom to testify the robustness of the proposed framework under different counting rates. The Monte Carlo simulation was designed to model the detector geometry and performance of the Hamamatsu SHR-22000 PET system.[46] The simulated template is a brain phantom with a size of 64 pixels × 64 pixels. The radio tracer is set to be ^{18}F-FDG and the total simulation time is 90 min divided into 30 time frames: 4 × 20s, 4 × 40 s, 4 × 60 s, 4 × 180 s, 14 × 300 s. The generated 2D sinogram has 64 × 64 projections at each time frame. The time-activity curves, as shown in Fig. 2(b), are generated based on the two-tissue compartment model with kinetic parameters K_1, k_2, k_3, and k_4 (min^{-1}) set as in Ref. [47]. Four sets of sinogram under different counting rates of 5×10^4, 1×10^5, 5×10^5, 1×10^6 have been created in total.

Shown in Figs. 3 and 4 are the visual results for the 9th and 13th frames of the image sequences from brain phantom data, respectively. From the top to the bottom, activity maps are achieved by MLEM, DE, and SDES, respectively. It is obvious that the MLEM image is heavily corrupted with noise when the counting rate is relatively small, whereas the SDES method maintains the image characteristics according to the ground truth. Also, when we compared the second and third lines of the images, the improvement in the quality can be visually recognized since the sharpness of the boundary is clearly improved. The improvements in image quality can be further confirmed in Table I, from which the efficiency of the clustering component in reducing noise corruption in the reconstructed PET image can be told from the decreased variance value.

Supplemental Fig. S5 is the estimation of parametric images under different counting rates through DE and SDES method. It can be speculated from the images that when the counting rates become lower, as in most dynamic PET compared to static PET scans, the noise corruption in the parameter estimation can still be tolerable when the counting rates are higher than 5×10^4 compared to the DE approach. Table II demonstrates the mean square error (MSE) of the parametric image of K_1. It can be noticed that within the range of counting rates that we have initialized, even the most corrupted data can achieve a better estimated parametric result through the SDES method.

Figure 5 represents the comparison of clustering results of SDES under different counting rates. To assess the cluster accuracy, we defined an evaluation criteria of symbol error rate (SER) representing the percentage of wrongly clustered pixels in the imaging field; the quantitative results are shown in Table III. Figure 5 shows that the results of clustering are highly influenced by the low counts. The result with 5×10^5 counting rate has the lowest SER (18.05%). When the counting rates are 5×10^4 and 1×10^5, one functional region in their images has disappeared even if their SERs are 20.34% and 19.21%, respectively.

4.B.2 Zubal thorax phantom

For the Zubal phantom data, as shown in Fig. 6(a), the size of the PET image sequence is 128 pixels × 128 pixels for all 18 time frames during the 60 min scanning. The time interval between each time frames is set as: 4 × 30 s, 4 × 120 s, 10 × 300s and the time-activity curves, as shown in Fig. 6(b), is generated based on the theory of two-tissue compartment model with the same set of kinetic parameters in Ref. [48]. The detector geometry and performance in the MonteCarlo simulation is the same as the brain phantom while the size of

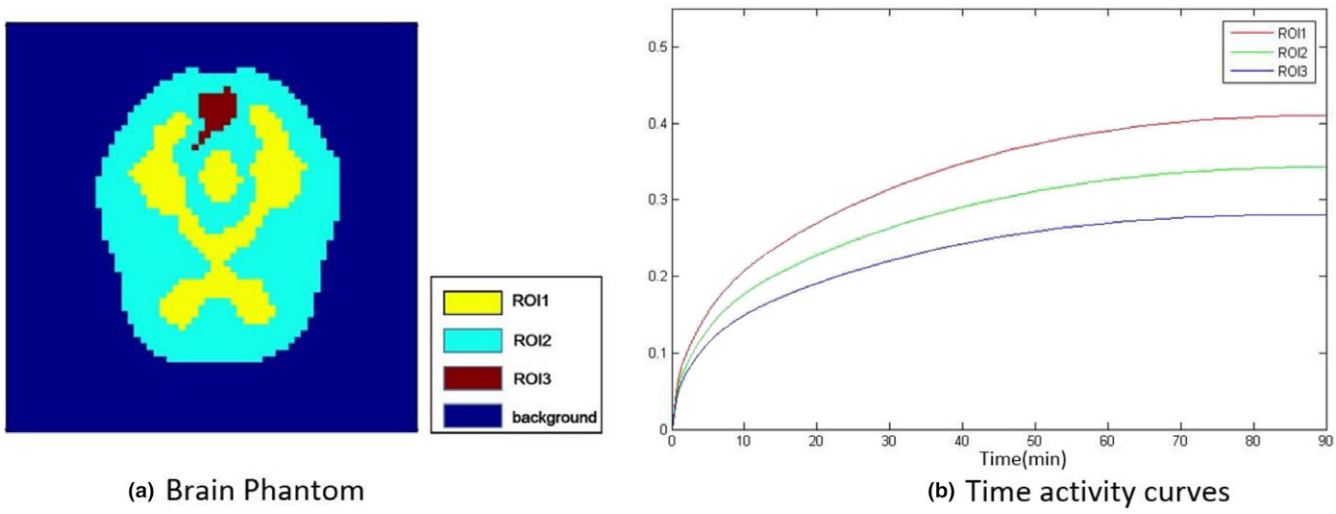

FIG. 2. Template and time-activity curves for the dataset of brain phantom. [Color figure can be viewed at wileyonlinelibrary.com]

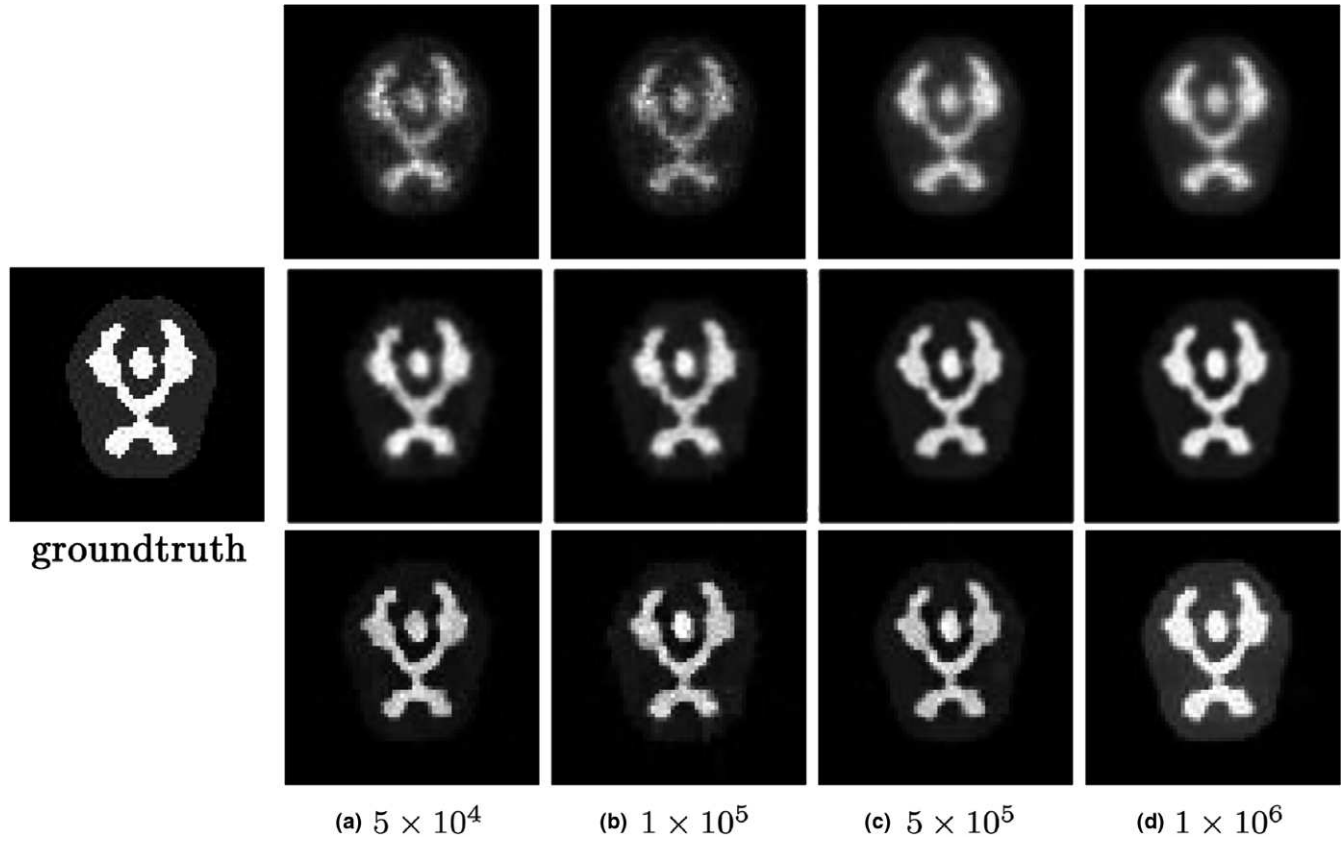

FIG. 3. Reconstruction of the 9th frame from PET image sequences for brain phantom data, from top to the bottom: MLEM, DE, and SDES methods.

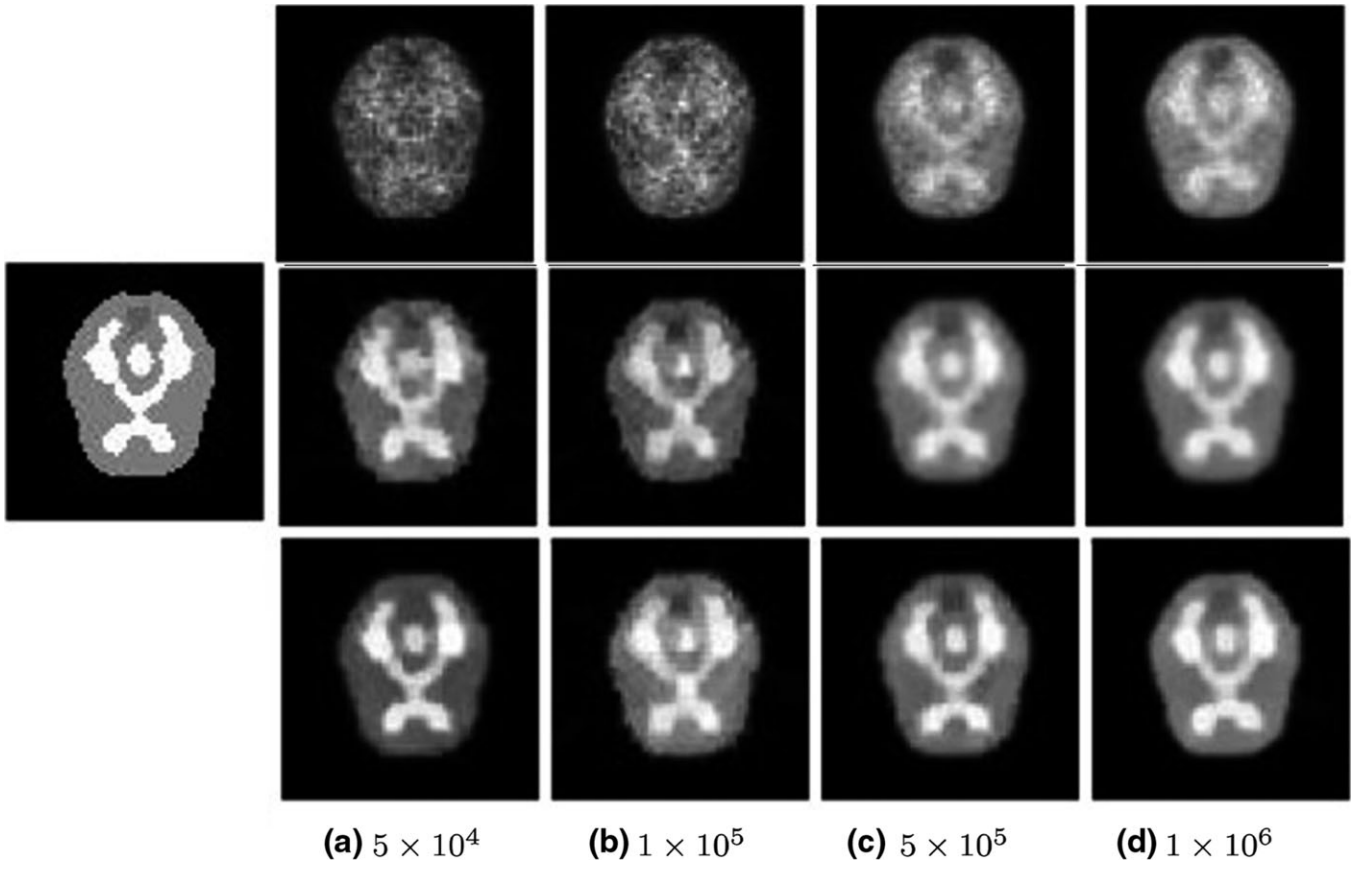

FIG. 4. Reconstruction of the 13th frame from PET image sequences for brain phantom data, from top to the bottom: MLEM, DE, and SDES methods.

TABLE I. Brain phantom: bias and variance results for each ROI (The minimum value for each ROI is in bold)

		Bias				Variance			
Counting Rate	Method	Whole	ROI1	ROI2	ROI3	Whole	ROI1	ROI2	ROI3
5×10^4	SDES	0.3909	0.2551	0.4452	0.3191	0.0809	0.1033	0.0735	0.0511
	DE	0.4752	0.2914	0.5511	0.3150	0.1356	0.0937	0.1529	0.1055
	MLEM	0.5220	0.5736	0.5062	0.4212	0.1626	0.1136	0.1836	0.0982
1×10^5	SDES	0.3162	0.2035	0.3626	0.2218	0.0576	0.0613	0.0570	0.0349
	DE	0.3773	0.2219	0.4394	0.2989	0.0874	0.0570	0.1005	0.0478
	MLEM	0.4772	0.5246	0.4624	0.3916	0.1367	0.1001	0.1527	0.0824
5×10^5	SDES	0.2312	0.1445	0.2651	0.2051	0.0393	0.0318	0.0432	0.0118
	DE	0.2422	0.1886	0.2625	0.2452	0.0685	0.0487	0.0774	0.0335
	MLEM	0.2494	0.3057	0.2269	0.2767	0.0761	0.0986	0.0689	0.0418
1×10^6	SDES	**0.1270**	**0.1093**	**0.1323**	0.1684	**0.0281**	**0.0192**	**0.0323**	**0.0068**
	DE	0.1511	0.1161	0.1639	**0.1662**	0.0326	0.0292	0.0347	0.0119
	MLEM	0.1637	0.2255	0.1383	0.2151	0.0410	0.0546	0.0359	0.0402

TABLE II. Relative MSE for the reconstructed K_1 from Monte Carlo-simulated data (The minimum value for each ROI is in bold)

	Zubal phantom		Brain phantom			
Method	5×10^4	1×10^5	5×10^4	1×10^5	5×10^5	1×10^6
SDES	**0.0394**	**0.0367**	**0.0424**	**0.0396**	**0.0369**	**0.0343**
DE	0.0636	0.0453	0.0546	0.0539	0.0436	0.0392
DEPICT	0.1248	0.0879	0.0663	0.0603	0.0481	0.0432

projection is $64 \times 64 \times 18$ time frames. In Zubal phantom case, there are only two different numbers of coincidence events (5×10^4, 1×10^5) that are simulated for comparison.

In Fig. 7, a comparison of 10th activity image frame between the SDES, DE, and the MLEM method is presented for different counting rates. According to the results, the noise levels and the associated resolution degradation in MLEM images are quite obvious, compared with the other two approaches, regardless of the counting rate levels. A specific difference in accuracy between SDES and DE can be found in quantitative results presented in Table IV. Compared with ground truth, the SDES method under higher counting rates achieves the most accurate results. The improvements in the variance between DE and SDES verify that the additional cluster part in the objective function can make the system less sensitive to the noise corruption. In the Table IV, the DE results of 5×10^4 counting rate are consistently superior to SDES at ROI 1. The reason might be that with the lower counting rates in ROI 1, the clustering is not effective thereby influencing the accuracy of reconstruction results. As for the parametric image of K_1, the visual profiles of horizontal and vertical lines across the image field are extracted in Supplementary Fig. 6 and the mathematical evaluation is presented in Table II. Lastly, Fig. 8 demonstrated the segmented images from different methods. Although compared with the other three results there is some noise in the SDES result, it shows the closest structure of ground truth, thus having the lowest SER (Table III).

TABLE III. SER for Monte Carlo-simulated data (The minimum value for each ROI is in bold)

Brain phantom (SDES)			
5×10^4	1×10^5	5×10^5	1×10^6
20.34%	19.21%	**18.05%**	18.11%
Zubal phantom (1×10^5)			
SDES	MLEM + KMC	DE + KMC	KSC
18.87%	23.81%	19.33%	22.38%

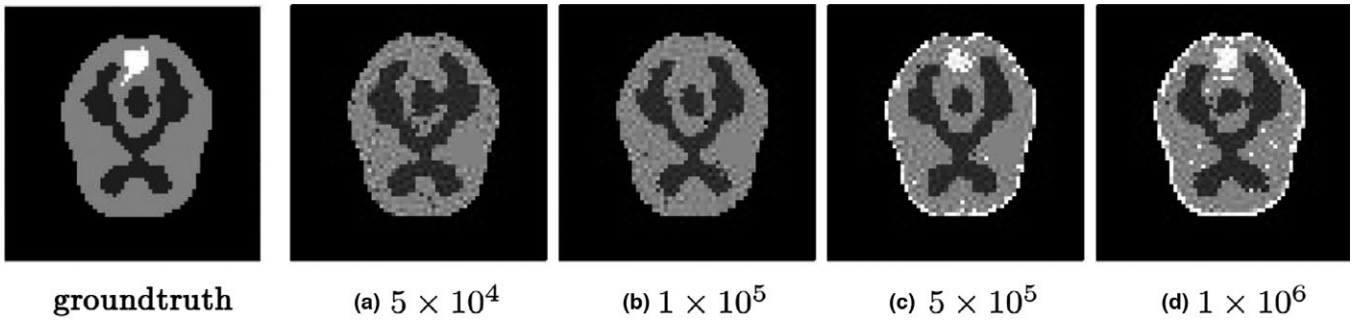

FIG. 5. Clustering results for the Hoffman brain phantom under different counting rates through the SDES method.

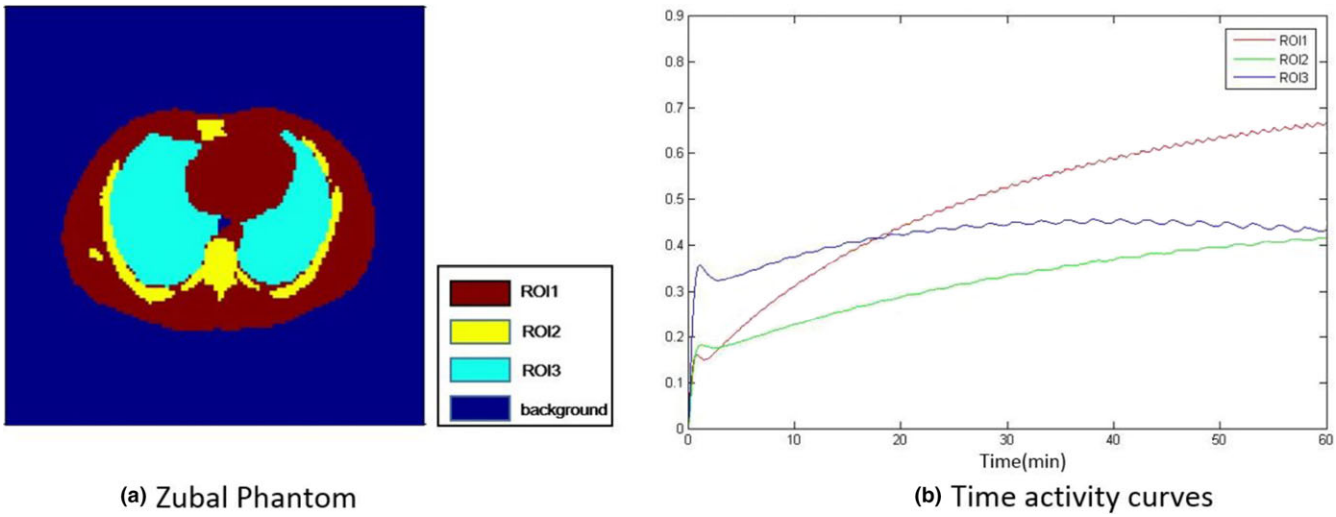

FIG. 6. Template and time-activity curves for the data set of Zubal thorax phantom. [Color figure can be viewed at wileyonlinelibrary.com]

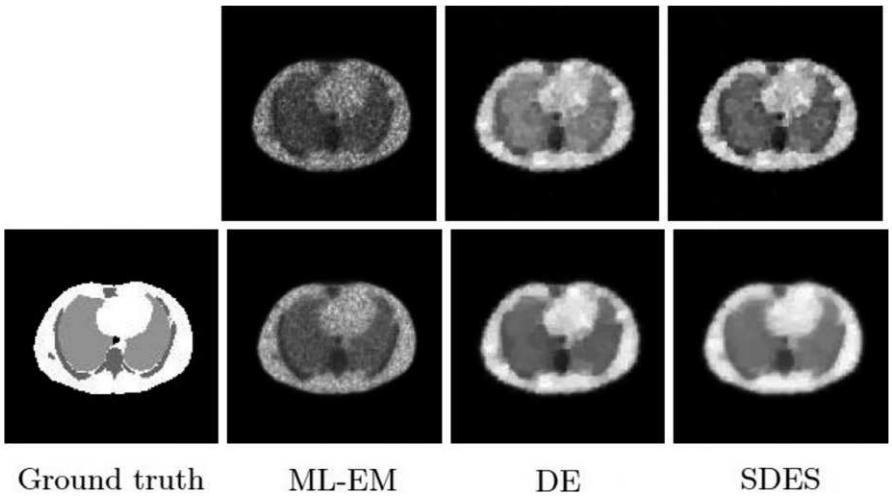

FIG. 7. Reconstruction of PET image sequences for Zubal phantom data: 10th frame. From top to the bottom: 5×10^4, 1×10^5.

4.C. Brain data with MR reference

A set of FDG-PET brain image sequence with registered MRI (magnetic resonance imaging) data has been used in this experiment. The estimated parameter images of K_1 is shown in Supplemental Fig. S7. From these images, it is shown that the SDES result has a clearer structure than DEPICT and DE. The reconstruction activity results of MLEM, DE, and SDES are shown in Fig. 9. Figure 9(a) shows a higher number of counts (5×10^7) in the PET images reconstructed by MLEM for reference. From top to bottom is the 14th frame and the 22nd frame. It can be seen

TABLE IV. Zubal phantom: bias and variance results for each ROI (The minimum value for each ROI is in bold)

		Bias				Variance			
Counting Rate	Method	Whole	ROI1	ROI2	ROI3	Whole	ROI1	ROI2	ROI3
5×10^4	SDES	**0.1765**	0.1737	**0.1589**	**0.1864**	**0.0425**	0.0447	**0.0828**	**0.0386**
	DE	0.2778	**0.1706**	0.5556	0.3751	0.0620	**0.0437**	0.1192	0.0814
	MLEM	0.5192	0.5249	0.4852	0.5198	0.2772	0.2837	0.2489	0.2750
1×10^5	SDES	**0.1559**	**0.1492**	**0.1574**	**0.1667**	**0.0354**	0.0368	**0.0423**	**0.0310**
	DE	0.1820	0.1540	0.2290	0.2151	0.0435	**0.0360**	0.0663	0.0495
	MLEM	0.3043	0.2992	0.3727	0.2925	0.0644	0.0365	0.1041	0.0997

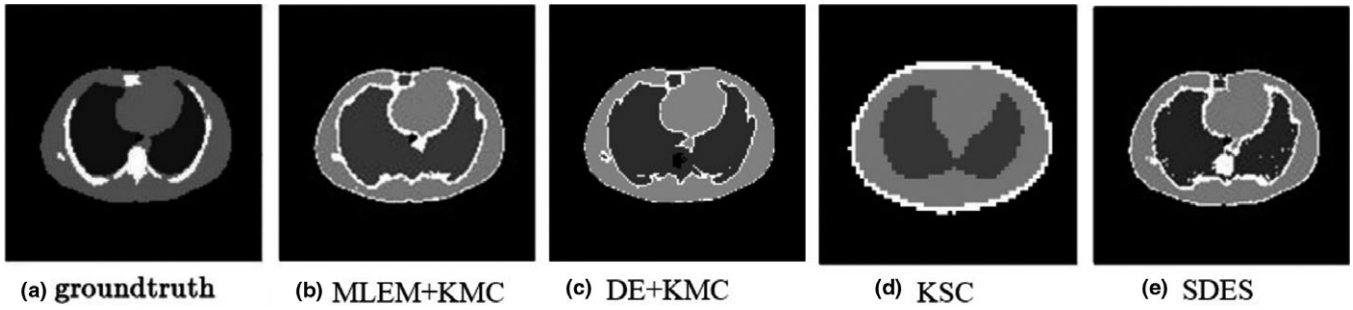

FIG. 8. Clustering results for the Zubal thorax phantom under the counting rate of 1×10^5.

that when counting rate is low in the 14th frame, the result of MLEM is very noisy while the edges of SDES appear subtly. Figure 10 shows the clustering results for MLEM + KMC, DE + KMC, and SDES methods. It seems the brain structure in the SDES result is close to reference image shown in Fig. 9(a), especially for paracele, which verifies its segmentation ability.

4.D. Cardiac data

The tracer injected into the cardiac patient is ^{18}F-FDG. The whole scan lasted 60 min and the raw measurement data were collected from 130×96 projections in 19 time frames.

Since the ground truth of the data cannot be defined, there are only visual results for the real patient data to demonstrate. Examples of reconstructed activity with blowup view at the 4th frame through SDES, DE, and MLEM method are given in Fig. 11. The boundary of the ventricle is more distinct in SDES than traditional MLEM method. Parametric images of K_1 are shown in Supplemental Fig. S8 with an even stronger contrast inside the ventricle. Figure 12 illuminated the functional regions presented through a clustering process in which KSC has specifically indicated the area of the ventricle while the other two clustered the whole imaging area into three functional regions.

5. DISCUSSION

Our current work is targeted at the joint PET image reconstruction and kinetic segmentation. The data-driven estimation of parametric images based on compartmental theory is implemented in this approach. When it comes to clinical practice, it should be noticed that the whole method is based on compartmental model assumption. It is assumed that each compartment is well mixed and the rate constants do not change with time.[50] Therefore, the results largely depend on

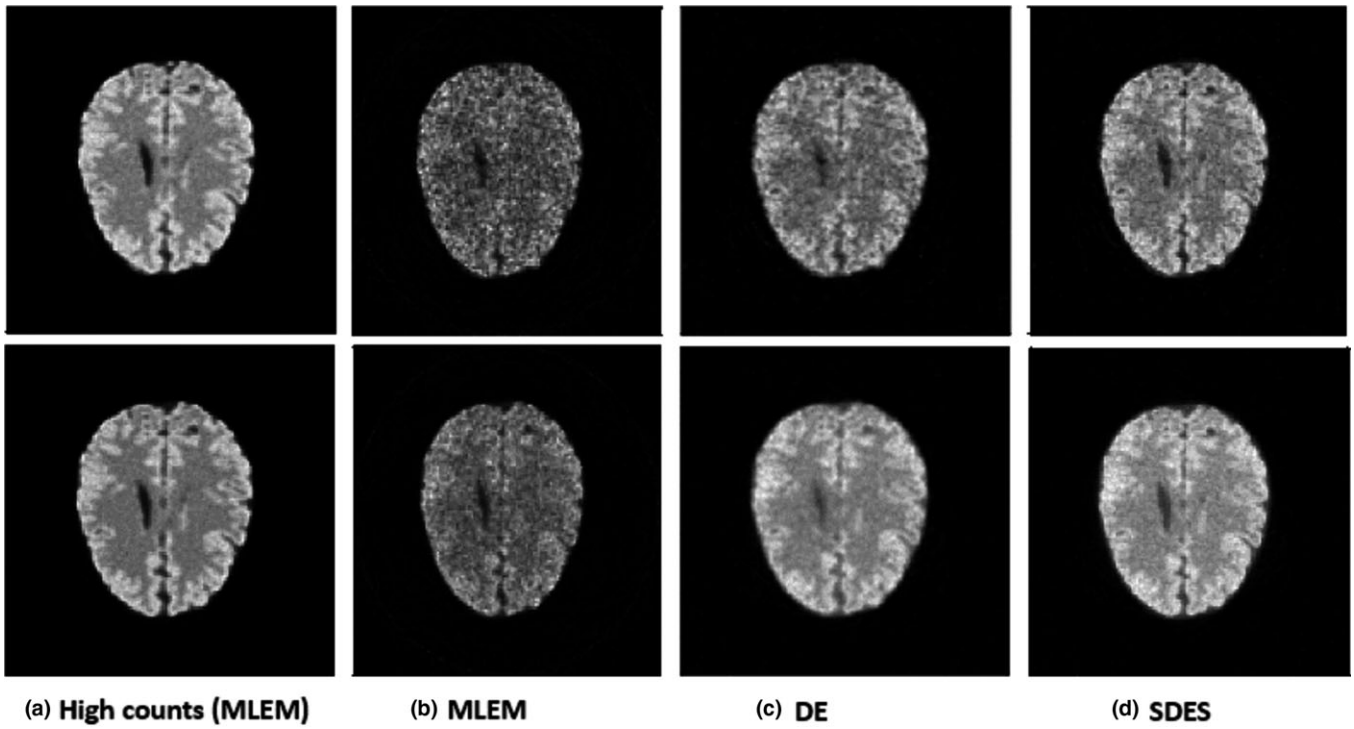

FIG. 9. (a) Higher number of counts (5×10^7) PET images reconstructed by MLEM for reference; (b–d) Reconstructed activity maps of MLEM, DE and SDES, from top to bottom: 14th frame, 22nd frame.

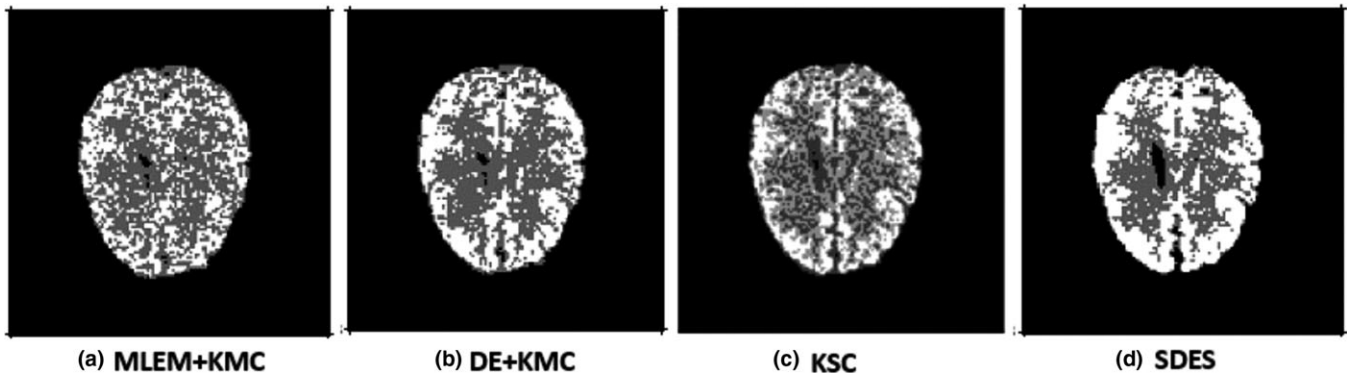

FIG. 10. Clustering results for MLEM + KMC, DE + KMC, and SDES methods.

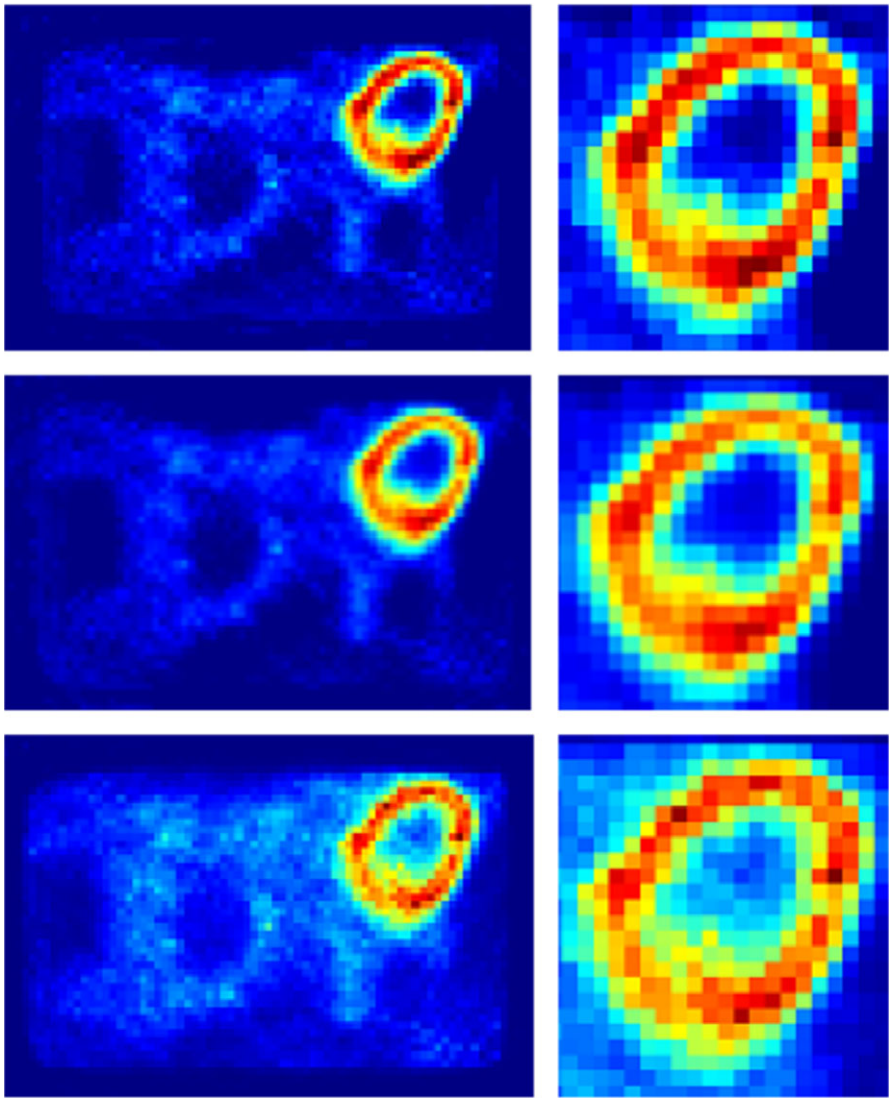

FIG. 11. The 4th frame reconstructed PET images for real patient data. From top to bottom: SDES, DE, and MLEM. On the right is the zoom in area of ventricle. [Color figure can be viewed at wileyonlinelibrary.com]

whether the compartmental model is similar to real case. In our method, the introduction of generalized compartmental spectral makes the data-driven estimation much closer to real situation.

Another limitation of our method is that the segmentation of dynamic PET data is according to a clustering of kinetic parameters on the strength of the assumption that physiological similarity of voxels in ROIs could be recognized by

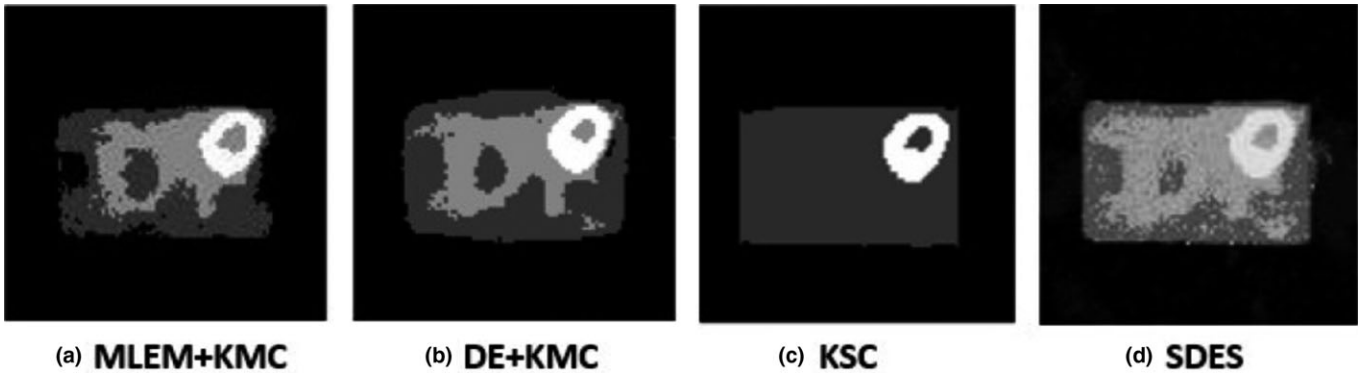

FIG. 12. Clustering results for the real patient data. Left to right: MLEM + KMC, DE + KMC, KSC, and SDES.

analyzing the similarity between their TACs. The work[34] demonstrated that segmentation methods implicitly allow for some clusters spreading away from their centroids. But when kinetic profiles overlap too much, the quality of cluster would be affected. This motivated us to choose a robust segmentation approach that can afford more spreading. In this paper, the Dirichlet process clustering was applied for its advanced performance. In addition, optimization of reconstruction parameters and movement correction should be done to minimize undesirable influences to the segmentation process.

There are certain limitations associated with our proposed implementation of the SDES method. First, there is a relatively large number of parameters to be tuned. For our study, we limited the parameters to a suitable range suggested by the current research approaches on the topics.[32,45] Although at present the proposed set of parameters is effective enough for a satisfied result, several experiments, during which the four parameters are slightly tuned, still need to be conducted before the validation of the SDES method. The other problem falls into the high computation cost of the algorithm. First, the problem is solved through an alternative optimizing scheme with respect to two variables and one auxiliary variable. When compared to MLEM method, the time complexity for MLEM method is $\mathcal{O}(N)$ (M-step) and for SDES is $\mathcal{O}(N^2)$(most time consuming process was in the update of the X variable). And more importantly, the clustering algorithm with a Dirichlet process applied for initialization is a time-consuming task owing to the strategy of determining the cluster labels pixel by pixel. Additionally, the number of clusters H should be prechosen by experience in the Dirichlet process.

For future work, we think it would be computationally promising to perform the clustering process on reasonably designed pixel patches, which would introduce spatial information and make the clustered ROIs less sensitive to noise corruption. And we would also try other advanced clustering methods to see whether it would have better results.

6. CONCLUSION

In this paper, we presented a joint reconstruction framework for simultaneously estimating the activity distribution, parametric images, and segmentation of the ROIs into different functional areas. Total variation regularization is performed on the activity distribution domain to suppress noise and preserve the edges between ROIs. In addition, a sparsity constraint for the coefficient matrix Φ is incorporated for the regression subproblem of selecting the most related subset from the overcomplete dictionary based on compartmental model theory. Another important feature is that the dictionary is data dependent since the time activity curve for the tissue is related to the tracer and different sampling times may lead to different concentration values. The experimental results presented in the previous sections demonstrated that the proposed method has lowest bias, variance, MSE, and SER compared to the MLEM, DEPICT, kinetic spectral clustering, and k-means methods.

ACKNOWLEDGMENT

This work is supported in part by National Key Technology Research and Development Program of China (No: 2017YFE0104000, 2016YFC1300302), by the National Natural Science Foundation of China (No: 61525106, 61427807, U180920013, 61701436, 81873908), by Shenzhen Innovation Funding (No: JCYJ20170818164343304, JCYJ2017081617 2431715), and NSF DMS1719932.

[a)]Author to whom correspondence should be addressed. Electronic mail: liuhf@zju.edu.cn.

REFERENCES

1. Lu L, Karakatsanis NA, Tang J, Chen W, Rahmim A. 3.5D dynamic PET image reconstruction incorporating kinetics-based clusters. *Phys Med Biol*. 2012;57:5035–5055.
2. Karakatsanis NA, Casey ME, Lodge MA, Rahmim A, Zaidi H. Whole-body direct 4d parametric pet imaging employing nested generalized patlak expectation–maximization reconstruction. *Phys Med Biol*. 2016;61:5456.
3. Karakatsanis NA, Lodge MA, Tahari AK, Zhou Y, Wahl RL, Rahmim A. Dynamic whole-body pet parametric imaging: I. Concept, acquisition protocol optimization and clinical application. *Phys Med Biol*, 2013;58:7391.
4. Zhu W, Li Q, Bai B, Conti PS, Leahy RM. Patlak image estimation from dual time-point list-mode pet data. *IEEE Trans Med Imaging*. 2014;33:913–924.

5. Avril N, Bense S, Ziegler SI, et al. Breast imaging with Fluorine-18-FDG PET: quantitative image analysis. *J Nucl Med*. 1997;38:1186–1191.
6. Dimitrakopoulou-Strauss A, Strauss LG, Heichel T, et al. The role of quantitative 18F-FDG PET studies for the differentiation of malignant and benign bone lesions. *J Nucl Med*. 2002;43:510–518.
7. Schmidt KC, Turkheimer FE. Kinetic modeling in positron emission tomography. *Q J Nucl Med Mol Imaging*. 2002;46:70.
8. Lin Y, Haldar JP, Li Q, Conti PS, Leahy RM. Sparsity constrained mixture modeling for the estimation of kinetic parameters in dynamic PET. *IEEE Trans Med Imaging*. 2014;33:173–185.
9. Lougovski A, Hofheinz F, Maus J, Schramm G, Hoff J. On the relation between Kaiser–Bessel blob and tube of response based modelling of the system matrix in iterative PET image reconstruction. *Phys Med Biol*. 2015;60:4209–4224.
10. Nguyen VG, Lee SJ. Incorporating anatomical side information into PET reconstruction using nonlocal regularization. *IEEE Trans Image Process*. 2013;22:3961–3973.
11. Rakvongthai Y, Ouyang J, Guerin B, Li Q, Alpert NM, El FG. Direct reconstruction of cardiac PET kinetic parametric images using a preconditioned conjugate gradient approach. *Med Phys*. 2013;40:10.
12. Cheng X, Li Z, Liu Z, et al. Direct Parametric Image Reconstruction in Reduced Parameter Space for Rapid Multi-Tracer PET Imaging. *IEEE Trans Med Imaging*. 2015;34:1498–1512.
13. Snyder DL. Parameter estimation for dynamic studies in emission-tomography systems having list-mode data. *IEEE Trans Nucl Sci*. 1984;31:925–931.
14. Kamasak ME, Bouman CA, Morris ED, Sauer K. Direct reconstruction of kinetic parameter images from dynamic PET data. *IEEE Trans Med Imaging*. 2005;24:636–650.
15. Yan J, Planeta-Wilson B, Carson RE. Direct 4-D PET list mode parametric reconstruction with a novel EM algorithm. *IEEE Trans Med Imaging*. 2012;31:2213–2223.
16. Wang G, Qi J. Generalized algorithms for direct reconstruction of parametric images from dynamic PET data. *IEEE Trans Med Imaging*. 2009;28:1717–1726.
17. Wang G, Qi J. An optimization transfer algorithm for nonlinear parametric image reconstruction from dynamic PET data. *IEEE Trans Med Imaging*. 2012;31:1977–1988.
18. Wang G, Qi J. Direct estimation of kinetic parametric images for dynamic PET. *Theranostics*. 2013;3:802–815.
19. Barber DC. The use of principal components in the quantitative analysis of gamma camera dynamic studies. *Phys Med Biol*. 1980;25:283–292.
20. Guo H, Renaut R, Chen K, Reiman E. Clustering huge data sets for parametric PET imaging. *Biosystems*. 2003;71:81–92.
21. Liptrot M, Adams KH, Martiny L, et al. Cluster analysis in kinetic modelling of the brain: a noninvasive alternative to arterial sampling. *NeuroImage*. 2004;21:483–493.
22. Jaouen V, Gonzalez P, Stute S, et al. Variational segmentation of vector-valued images with gradient vector flow. *IEEE Trans Image Process*. 2014;23:4773–4785.
23. Reader AJ, Sureau FC, Comtat C, Trébossen R, Buvat I. Joint estimation of dynamic PET images and temporal basis functions using fully 4D ML-EM. *Phys Med Biol*. 2006;51:5455–5474.
24. Saad A, Smith B, Hamarneh G, Möller T. Simultaneous segmentation, kinetic parameter estimation, and uncertainty visualization of dynamic PET images. In: *Medical Image Computing and Computer-Assisted Intervention–MICCAI*. Heidelberg, Springer; 2007:726–733.
25. Krestyannikov E, Tohka J, Ruotsalainen U. Joint penalized-likelihood reconstruction of time-activity curves and regions-of-interest from projection data in brain PET. *Phys Med Biol*. 2008;53:2877–2896.
26. Yoon S, Pineda AR, Fahrig R. Simultaneous segmentation and reconstruction: a level set method approach for limited view computed tomography. *Med Phys*. 2010;37:2329–2340.
27. Teh YW, Jordan MI, Beal MJ, Blei DM. Sharing clusters among related groups: Hierarchical dirichlet processes. In: *Advances in Neural Information Processing Systems*. 2005:1385–1392.
28. Vardi Y, Shepp LA, Kaufman L. A statistical model for positron emission tomography. *J Am Stat Assoc*. 1985;80:8–20.
29. Shepp LA, Vardi Y. Maximum likelihood reconstruction for emission tomography. *IEEE Trans Med Imaging*. 1982;1:113–122.
30. Rudin LI, Osher S, Fatemi E. Nonlinear total variation based noise removal algorithms. *Physica D*. 1992;60:259–268.
31. Gunn RN, Gunn SR, Cunningham VJ. Positron emission tomography compartmental models. *J Cereb Blood Flow Metab*. 2001;21:635–652.
32. Gunn RN, Gunn SR, Turkheimer FE, Aston JA, Cunningham VJ. Positron emission tomography compartmental models: a basis pursuit strategy for kinetic modeling. *J Cereb Blood Flow Metab*. 2002;22:1425–1439.
33. Cheng-Liao J, Qi J. Segmentation of mouse dynamic PET images using a multiphase level set method. *Phys Med Biol*. 2010;55:6549.
34. Mouysset S, Zbib H, Stute S, et al. Segmentation of dynamic PET images with kinetic spectral clustering. *Phys Med Biol*. 2013;58:6931.
35. Elhamifar E, Vidal R. Sparse subspace clustering: algorithm, theory, and applications. *IEEE Trans Pattern Anal Mach Intell*. 2013;35:2765–2781.
36. Duda RO, Hart PE, Stork DG. *Pattern Classification*. John Wiley & Sons; 2012.
37. Neal RM. Markov chain sampling methods for Dirichlet process mixture models. *J Comput Graph Stat*. 2000;9:249–265.
38. Frigyik BA, Kapila A, Gupta MR. Introduction to the Dirichlet distribution and related processes. *Department of Electrical Engineering, University of Washington, UWEETR-2010-0006*; 2010.
39. Gabay D, Mercier B. *A Dual Algorithm for the Solution of Non Linear Variational Problems Via Finite Element Approximation*. Institut de recherche d'informatique et d'automatique; 1975.
40. Glowinski R. Marroco A. Sur l'approximation, par éléments finis d'ordre un, et la résolution, par pénalisation-dualité d'une classe de problèmes de dirichlet non linéaires. *Rev Fran¸ caised'Automatique, Informatique, Rech Op'erationelle*. 1975;9:41–76.
41. Zhang H, Hager WW. A nonmonotone line search technique and its application to unconstrained optimization. *SIAM J Optim*. 2004;14:1043–1056.
42. Barzilai J, Borwein JM. Two-point step size gradient methods. *IMA J Num Anal*. 1988;8:141–148.
43. Ng AY, Jordan MI, Weiss Y. On Spectral Clustering: analysis and an algorithm. In: *Proceedings of Advances in Neural Information Processing Systems*. Vol. 28. Cambridge, MA: MIT Press; 2001: 849–856.
44. Rosasco L, Verri A, Santoro M, Mosci S, Villa S. *Iterative projection methods for structured sparsity regularization. MIT technical reports. MIT-CSAIL-TR-2009-050*; 2009.
45. Li C, Yin W, Zhang Y. Users guide for TVAL3: TV minimization by augmented Lagrangian and alternating direction algorithms. CAAM report. 2009;20:46–47.
46. Tian Y, Katabe A, Liu H-F, Bao C, Yamashita T. Performance evaluation of the HAMAMATSU SHR22000 whole-body PET scanner using the IEC standard. *High Energy Phys Nucl Phys*. 2006;30:1123–1127.
47. Spence AM, Muzi M, Mankoff DA, et al. 18F-FDG PET of gliomas at delayed intervals: improved distinction between tumor and normal gray matter. *J Nucl Med*. 2004;45:1653–1659.
48. Tong S, Shi P. Tracer kinetics guided dynamic PET reconstruction. In: *Information Processing in Medical Imaging*. Heidelberg: Springer; 2007:421–433.
49. Kanungo T, Mount DM, Netanyahu NS, Piatko CD, Silverman R, Wu AY. An efficient k-means clustering algorithm: analysis and implementation. *IEEE Trans Pattern Anal Mach Intell*. 2002;24:881–892.
50. Carson, RE. Tracer kinetic modeling in PET. In: *Positron Emission Tomography*. London: Springer; 2005:127–159.
51. Cocosco CA, Kollokian V, Kwan RKS, Pike GB Evans AC. Brainweb: online interface to a 3D MRI simulated brain database. *NeuroImage*; 1997.

SUPPORTING INFORMATION

Additional supporting information may be found online in the Supporting Information section at the end of the article.

Figure S1. Profile of 44th column, 10th frame of PET image under different choice of $\alpha \in \{2^5, 2^6, 2^{6.5}, 2^7, 2^8\}$.

Figure S2. (a) and (b) are the relative bias, variance, and MSE under different choices $\gamma \in \{0.1, 0.33, 0.66, 1, 1.33, 1.66, 2.33\}$.

Figure S3. Profile of 44th column, 10th frame of PET image under different choice of $\mu \in \{0.01, 0.03, 0.06, 0.10\}$.

Figure S4. Profile of 44th column, 10th frame of PET image under different choice of $\epsilon \in \{0.5, 1, 2, 3\}$.

Figure S5. Reconstruction of parametric images K_1 for brain phantom data under different counting rates. From top to bottom: DE and SDES.

Figure S6. Profiles of the estimated parametric images for K_1.

Figure S7. Reconstructed parametric images of K_1. (a) Registration MRI image. (b) parametric images from DEPICT method. (c) parametric images from DE method. (d) parametric images from SDES method.

Figure S8. Parametric images of K_1 for real patient data. (a) MLEM; (b) DE and (c) SDES.

Measure and Evaluate MRgRT 3D Distortion

distortion check

CLOUD SOFTWARE FOR EVALUATION OF IMAGE DISTORTION

SCAN

UPLOAD IMAGES

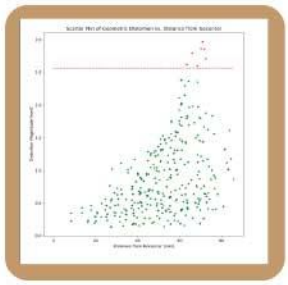

REVIEW REPORTS & TREND ANALYSIS

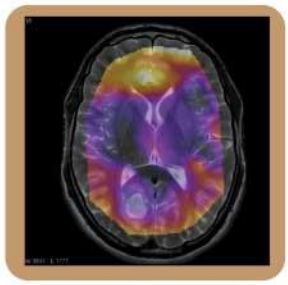

EXPORT DICOM OVERLAYS TO TPS

- CIRS proprietary materials simulate distortion due to susceptibility & chemical shifts typical to clinical patient scans

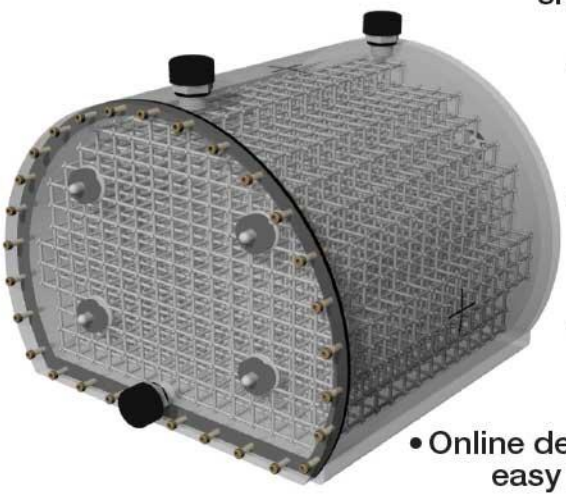

- Density of physical control points optimized to bring interpolation close to linearity
- Cloud based solution frees user of operating system and hardware constraints
- Quickly & automatically analyze complete MR data sets
- Online deployment facilitates collaboration, easy review and portability of results

Large Field Grid Phantom
2623 Physical Control Points

Visit us at ECR, Booth 128!

Inter-cranial Grid Phantom
335 Physical Control Points

CIRS

900 Asbury Ave. • Norfolk, Virginia 23513 • USA • Tel: 757-855-2765 • **WWW.CIRSINC.COM**